ELSEVIER

International Journal of Heat and Fluid Flow 22 (2001) 323–331

International Journal of
HEAT AND
FLUID FLOW

www.elsevier.com/locate/ijhff

# Large eddy simulation for turbulent buoyant flow in a confined cavity

Shia-Hui Peng *, Lars Davidson

*Department of Thermo and Fluid Dynamics, Chalmers University of Technology, SE-412 96 Gothenburg, Sweden*

**Abstract**

A turbulent natural convection flow ($Ra = 1.58 \times 10^9$) in a confined cavity with two differentially heated side walls was numerically investigated by means of large eddy simulation (LES). The mean flow in the cavity is characterized by stable thermal stratification and a relatively low turbulence level. The LES results for the mean flow quantities show good agreement with the experiment. This is particularly the case when the dynamic model is used. Nevertheless, there are some discrepancies in the prediction of turbulence statistics, particularly in the outer region of the near-wall flow where the boundary layer interacts with the recirculating core region. In the viscous/conductive sublayer of the boundary layer close to the heated/cooled vertical walls, the flow tends to form streak-like structures, which do not however emerge in the near-wall flow along the horizontal top and bottom walls. To resolve the flow structure near the vertical walls, sufficient grid resolution is required. 

*Keywords:* Large eddy simulation; Subgrid-scale model; Buoyant flow; Cavity

## 1. Introduction

Turbulent natural convection arising in a confined enclosure with two differentially heated side walls has been an attractive subject in fundamental turbulence research. In this configuration, the buoyancy is the only driving force for fluid motion and imposes significant effects on the turbulence evolution in the near-wall boundary layer. This type of flow is also of interest in industrial applications, for example, in the cooling of electrical equipment, solar energy collectors and building ventilation. A number of numerical studies on this type of flow have been carried out using Reynolds-averaged Navier–Stokes (RANS) approaches and have been based on a two-dimensional flow configuration, see e.g., Henkes and Hoogendoorn (1995), Dol et al. (1997) and Peng and Davidson (1999).

In addition to RANS modeling, large eddy simulation has attracted great attention and been increasingly implemented in computing turbulent buoyant flows. Various subgrid-scale (SGS) models have been used and shown encouraging performance, in which the study and comparison have usually been subjected to the atmospheric boundary layer for meteorological and environmental flows (Deardorff, 1973; Manson, 1989; Moeng and Rotunno, 1990) and to the well known Rayleigh–Bénard (RB) convection arising between two horizontal infinite planes (e.g., Cabot, 1992; Canuto et al., 1997; Peng and Davidson, 1998a). The RB convection in the turbulent regime is characterized by two distinct scales of motion: large-scale coherent vortical structure associated with plumes, thermals and convective cells that rise from the outer edge of the boundary layer, and the turbulence generated mainly in the wall boundary layer and carried away by the large-scale structure. Such a large-structure flow feature makes the RB convection particularly suitable to the use of large eddy simulation (LES), indicating one of the reasons for the visible success of LES when applied to this type of flow.

Unlike RB convection, turbulent buoyant cavity flow is often characterized by the formation of boundary layers along the enclosure surfaces with an encircled recirculating core region. The boundary layer interacts with the wall shear as well as with the core region that may take various patterns in the form of one or more rolls depending on the wall condition and the magnitude of the Rayleigh number. A large span of scales interacts with each other, introducing difficulties in the numerical solution. Based on Cheesewright's experiment (Cheesewright et al., 1986), some attempts have been made to perform large eddy simulations of a buoyant cavity flow (Peng and Davidson, 1998b). The results were however less satisfactory in comparison with the experimental data. Apart from the grid resolution, one of the main reasons was argued to be due to the failure of the SGS model used to capture the underlying physics of the energy backscatter phenomenon, which is regarded as an essential ingredient in reproducing the transition regime in the boundary layer near the vertical heated/cooled wall.

This work presents a numerical investigation of a turbulent buoyant cavity flow at a relatively low Rayleigh number, $Ra = 1.58 \times 10^9$. The flow was experimentally identified as being characterized by overall low turbulence, and no visible transition was detected in the boundary layer along the heated/cooled vertical walls (Tian, 1997). This makes a reasonable LES possible when using a computationally affordable grid resolution. It is expected that a detailed exploration of this

* Corresponding author. Tel.: +46-31-772-1413; fax: +46-31-18-0976.
*E-mail address:* peng@tfd.chalmers.se (S.-H. Peng).

0142-727X/01/$ - see front matter 
PII: S0142-727X(01)00095-9

type of flow will shed light on the flow physics and give some implications for further SGS modeling of turbulent buoyant flows. The simulation is compared with experimental data. The performance of the SGS model used is discussed, and the near-wall flow features are analyzed.

## 2. Simulation methodology

### 2.1. The subgrid-scale models

Filtering the Navier–Stokes equations and the thermal energy equation in space leads to unknown SGS stresses and heat fluxes in the filtered equations, respectively. They represent the effect of the subgrid scales on the large-scale eddies and must be modeled so as to resolve the large-scale motion. The SGS stresses appearing in the filtered Navier–Stokes equations are responsible for the occurrence of energy between the large-scale and the subgrid-scale eddies. They have often been modeled in alignment with the resolved, large-scale strain rate, $\bar{S}_{ij} = (1/2)((\partial\bar{u}_i/\partial x_j) + (\partial\bar{u}_j/\partial x_i))$, by means of the SGS eddy viscosity, $v_t$, viz.

$$\tau_{ij} = \overline{u_i u_j} - \bar{u}_i\bar{u}_j = -2v_t\bar{S}_{ij} + \frac{\delta_{ij}}{3}\tau_{kk}. \tag{1}$$

Using the gradient diffusion hypothesis, the SGS heat flux vector, $h_j$, in the filtered thermal energy equation is modeled as

$$h_j = \overline{\theta u_j} - \bar{\theta}\bar{u}_j = -\alpha_t\frac{\partial\bar{\theta}}{\partial x_j}, \tag{2}$$

where $\alpha_t = v_t/Pr_t$ is the SGS diffusivity and $Pr_t$ is the SGS Prandtl number.

The SGS viscosity has often been formulated in terms of the filter width, $\Delta$, and a time scaling quantity, $\mathscr{T}$, i.e., $v_t \propto \Delta^2/\mathscr{T}$. In the well known Smagorinsky (1963) model, this time scaling is set to be equal to the reciprocal of the magnitude of the resolved strain rate tensor, $|\bar{S}| = \sqrt{2\bar{S}_{ij}\bar{S}_{ij}}$, giving

$$v_t = C\frac{\Delta^2}{\mathscr{T}} = C\Delta^2|\bar{S}|. \tag{3}$$

Consequently, the SGS eddy diffusivity can be written as

$$\alpha_t = C_t\frac{\Delta^2}{\mathscr{T}} = \frac{C}{Pr_t}\Delta^2|\bar{S}|. \tag{4}$$

For isothermal turbulent flows, the $v_t$ formulation in (3) suggests that a local-equilibrium holds for the SGS eddies between the dissipation rate and the shear production of SGS kinetic energy. For natural convection flows where the buoyancy plays a significant role, Eidson (1985) proposed including the SGS buoyant production in the local-equilibrium argument. As a consequence, the SGS time scaling takes the following form:

$$\mathscr{T} = \left(|\bar{S}|^2 - \frac{g\beta}{Pr_t}\frac{\partial\bar{\theta}}{\partial x_j}\delta_{2j}\right)^{-1/2}. \tag{5}$$

To avoid rendering non-real solutions from this scaling, it is often necessary to constrain the instantaneous SGS viscosity to be equal to zero as $|\bar{S}|^2 < (g\beta/Pr_t)(\partial\bar{\theta}/\partial x_j)\delta_{2j}$, particularly for solving thermally stratified flows. This constraint can be relaxed by using $|\bar{S}|$ to weight the Eidson time scaling, as done by Peng and Davidson (1998a)

$$\mathscr{T} = \left(|\bar{S}| - \frac{g\beta}{Pr_t|\bar{S}|}\frac{\partial\bar{\theta}}{\partial x_j}\delta_{2j}\right)^{-1}. \tag{6}$$

Nevertheless, the use of (6) requires a "clipping" in the total viscosity, $(v_t + v)$, which should not be negative to retain numerical stability. Unlike the Eidson model, the SGS viscosity computed from (6) allows negative values of $v_t$ in the range of $[0,-v]$. For isothermal flows, both (5) and (6) return to the conventional Smagorinsky time scaling.

Model coefficients, $C$ and $C_t$, have been determined using the dynamic procedure (Germano et al., 1991; Lilly, 1992). The test filter, denoted by a curved overbar has a width of $\widehat{\Delta} = 2\Delta$, as proposed by Germano et al. (1991) to extrapolate the information from the smallest resolved scales. We have computed the grid filter width from $\Delta = (\Delta_x\Delta_y\Delta_z)^{1/3}$ in this work using box filter based on the finite-volume method, and where $\Delta_x$, $\Delta_y$ and $\Delta_z$ are the size of the control volume in the three directions, respectively.

The Germano identity for the SGS stress tensor reads

$$\mathscr{L}_{ij} = T_{ij} - \widehat{\tau_{ij}} = \widehat{\bar{u}_i\bar{u}_j} - \widehat{\bar{u}_i}\widehat{\bar{u}_j}. \tag{7}$$

For the heat fluxes, a similar identity holds as

$$\mathscr{E}_j = H_j - \widehat{h_j} = \widehat{\bar{u}_j\bar{\theta}} - \widehat{\bar{u}_j}\widehat{\bar{\theta}}. \tag{8}$$

On the test filtering level, both the stress tensor, $T_{ij}$, and the heat flux vector, $H_j$, are modeled respectively in analogy to their counterparts on the grid filtering level. Denoting the reciprocal of the time scale, $\mathscr{T}$, in the above models by $\bar{\omega}$, viz., $\bar{\omega} = 1/\mathscr{T}$, Eqs. (7) and (8) can then be written as, respectively,

$$\mathscr{L}_{ij} = -2C\widehat{\Delta}^2\widehat{\bar{\omega}}\widehat{\bar{S}}_{ij} + 2C\Delta^2\widehat{\bar{\omega}\bar{S}_{ij}} \tag{9}$$

and

$$\mathscr{E}_j = C_t\widehat{\Delta}^2\widehat{\bar{\omega}}\frac{\partial\widehat{\bar{\theta}}}{\partial x_j} - C_t\Delta^2\widehat{\bar{\omega}}\frac{\partial\bar{\theta}}{\partial x_j}, \tag{10}$$

where $C$ and $C_t$ have been assumed to be independent of the test-filtering operation.

By means of the least-square approach (Lilly, 1992), the model coefficient $C$ can be determined as

$$C = -\frac{\mathscr{L}_{ij}M_{ij}}{2M_{ij}M_{ij}}; \quad M_{ij} = \widehat{\Delta}^2\widehat{\bar{\omega}}\widehat{\bar{S}}_{ij} - \Delta^2\widehat{\bar{\omega}\bar{S}_{ij}}. \tag{11}$$

Similarly, the coefficient $C_t$ is determined by the following expression:

$$C_t = \frac{\mathscr{E}_jQ_j}{Q_jQ_j}; \quad Q_j = \widehat{\Delta}^2\widehat{\bar{\omega}}\frac{\partial\widehat{\bar{\theta}}}{\partial x_j} - \Delta^2\widehat{\bar{\omega}}\frac{\partial\bar{\theta}}{\partial x_j}. \tag{12}$$

To avoid numerical instability in the solution procedure, the model coefficients are assumed to be functions of time and of inhomogeneous directions. A spatial averaging for the numerators and denominators in (11) and (12) are thus made over the direction of flow homogeneity (if any). The SGS Prandtl number, $Pr_t$, can also be dynamically determined with different approaches as a function of time and space (Cabot, 1992; Peng and Davidson, 1998a). When the base model with constant model coefficients is employed for comparison, we have used $C = 0.0441$ and $Pr_t = 0.4$, as recommended by Eidson (1985).

### 2.2. Numerical Method

The governing equations are discretized on a collocated grid using the second-order central differencing finite-volume method (Davidson, 1997). An implicit, fractional step method is used to solve the discretized equations constructed in a parallelized code on Silicon Graphics ORIGIN 2000 machines. The solution is advanced in time using the second-order

Crank–Nicolson scheme. The filtered Navier–Stokes equation is discretized as follows:

$$\bar{u}_i^{n+1} = \bar{u}_i^n + \Delta t H\left(\bar{u}_i^n, \bar{u}_i^{n+1}, \bar{b}_i^n\right) - \frac{1}{\rho}\alpha\Delta t\frac{\partial \bar{p}^{n+1}}{\partial x_i} - \frac{1}{\rho}(1-\alpha)\Delta t\frac{\partial \bar{p}^n}{\partial x_i}, \tag{13}$$

where $\alpha = 0.5$, $H(\bar{u}_i^n, \bar{u}^{n+1}, \bar{b}_i^n)$ includes the convection, the viscous and SGS stresses and the buoyancy term, $\bar{b}_i^n$, in the gravitational direction, and $\Delta t$ is the time step. The thermal energy equation has been discretized in a similar manner. These discrete equations are solved using a symmetric Gauss–Seidel method. To reinforce the pressure–velocity coupling, an intermediate velocity field is computed by subtracting the implicit part of the pressure gradient from (13), giving

$$\bar{u}_i^* = \bar{u}_i^{n+1} + \frac{1}{\rho}\alpha\Delta t\frac{\partial \bar{p}^{n+1}}{\partial x_i}. \tag{14}$$

Taking the divergence of (14) leads to a Poisson equation for the pressure, i.e.,

$$\frac{\partial^2 \bar{p}^{n+1}}{\partial x_i \partial x_i} = \frac{\rho}{\alpha\Delta t}\frac{\partial \bar{u}_i^*}{\partial x_i}. \tag{15}$$

On the right-hand side of (15), the divergence of the velocity is computed from the velocities at the volume faces. The Poisson equation is solved using a multigrid method. The resulting pressure field, together with the intermediate velocities calculated from (14), is then used to correct the velocities at the volume faces. The filtered thermal energy equation is then solved, and the SGS eddy viscosity is subsequently computed.

## 3. Results and discussion

The natural convection flow was measured by Tian (1997) in an air-filled cavity with dimensions of $W = D/2$, $H = D/2$ and $D$ in the $x$, $y$ and $z$ directions. The two opposite vertical walls, located at $x = 0$ (hot wall) and $x = W$ (cold wall), respectively, were maintained isothermal with two water chambers, giving a temperature difference of $\Delta\Theta = 40$ K. The Rayleigh number, $Ra = (g\beta\Delta\Theta H^3 Pr)/\nu^2$ is $1.58 \times 10^9$. The wall surface temperatures were measured using K-type thermocouples. An E-type thermocouple was used to measure the air temperature in the cavity using a computer controlled displacement device to locate the measurement point. The temperature was read by a 16-bit data logging card at 50 Hz sample rate. For every location, 4096 readings were taken. The accuracy of the measuring location was disclosed to be better than 0.2 mm and the temperature reading was true within 0.1 K. A backscatter, two-dimensional laser doppler anemometer (LDA) was used in velocity measurements. The measured velocity range was $\pm 0.5082$ m/s with a resolution of $6.2 \times 10^{-5}$ m/s at a bandwidth of 0.125 MHz. A detailed description on the experimental measurement can be found in Tian (1997). The flow was experimentally identified as being characterized by low turbulence, and no visible transition was detected in the boundary layer along the heated/cooled vertical walls. The bottom (at $y = 0$) and top (at $y = H$) walls are highly conducting boundaries. Through a well controlled experimental setup, it was claimed that the cavity offers a two-dimensional mean flow in the middle section of the spanwise direction (at $z = D/2$), where the measurements had been made.

In the numerical computation, a no-slip condition was employed for the velocities and Neumann condition for the pressure on the wall surface. The thermal condition on the conducting top and bottom walls has been specified in accordance with the experimental measurements. Two types of boundary condition have been tested in the spanwise ($z$) direction: using a periodic boundary condition to approach a statistically two-dimensional simulation (hereafter Case 1); and specifying no-slip and adiabatic wall conditions to identify three-dimensional effects (hereafter Case 2). A grid with $96 \times 96 \times 64$ meshes was used under both conditions. The grid is stretched near the wall in both the $x$ and $y$ directions, typically, with 12–13 nodes clustered within $y^+ \leqslant 10$ near the vertical and horizontal walls.

When a periodic flow is assumed in the spanwise direction (Case 1), a uniform grid is employed and only half of the experimental cavity depth ($z_{\max} = D/2$) is taken for the numerical domain. This gives a resolution of $\Delta z^+ \approx 32$ based on the wall friction velocity at the mid-height ($y = H/2$) of the vertical boundary layer. It should be noted that, in this case, the computational domain in the spanwise direction should be at least twice as large as those of the largest turbulence scales. The correlation functions were thus checked. It was found that the correlation decays indeed to very small values over a distance of half of the domain size, $z_{\max}/2$. This suggests that the spanwise domain size, $z_{\max} = D/2$, is large enough to assume a periodic boundary condition in the computation. When the wall condition is specified in the spanwise direction (Case 2), for which the numerical domain is identical to the experimental setup ($z_{\max} = D$), a moderately clustered near-wall grid is utilized in the spanwise direction. The time step used in all computations is $\Delta t = 0.0131 t_0$, where $t_0 = H/\sqrt{g\beta\Delta\Theta H}$. The results shown below were averaged with respect to time and, for Case 1, also the homogeneous spanwise direction, denoted as $\langle\rangle$. The averaging time to obtain the statistic quantities is typically $(450\text{–}600)t_0$.

For all the simulations, it was found that the dynamic Smagorinsky model reproduces nearly identical results to those given by the dynamic modified buoyancy model, Eq. (6). It seems that the dynamic procedure is able to self-adjust the SGS viscosity to a similar level with both base models, or the strain-related term is generally larger than the buoyancy-related term in (6) for the case considered. In the following comparison, the results of the dynamic model are based on the modified buoyancy model in which Eq. (6) is used for the SGS time scaling.

Fig. 1 shows the distributions of mean velocity and temperature at three different locations, $y/H = 0.2$, 0.5 and 0.8, respectively. The experimental data for other flow quantities have fairly good antisymmetric distributions, but the distribution of the measured mean temperature was slightly disturbed. The profiles for the mean temperature near both the hot and cold walls are thus plotted, respectively, in Figs. 1(b) and (c). The buoyant velocity, $U_0 = \sqrt{g\beta\Delta\Theta H}$, the cold wall temperature, $\theta_{cw}$, and $\Delta\Theta$ have been used as normalization parameters. The results computed with the dynamic model are based on the periodic boundary condition in the spanwise direction, i.e., Case 1. To reveal the effect of the spanwise grid resolution, the results obtained with a $96 \times 96 \times 32$ grid (z32) are also shown when using the same dynamic model in this case. The coarse grid reproduces a slightly more narrow vertical boundary layer with a relatively large velocity peak as compared with the fine grid resolution, $96 \times 96 \times 64$ mesh (z64), in the spanwise direction of flow homogeneity.

For comparison, a group of results computed with the Smagorinsky model for Case 2 (i.e., no-slip and adiabatic wall conditions are specified on the spanwise boundaries) is also presented in Fig. 1. The distributions have been taken from the $z = D/2$ plane without performing spatial averaging. It should be noted that the Smagorinsky model used here has been modified by multiplying a van Driest-type damping function, $f_\mu = [1 - \exp(-y^+/25)]^2$, to the model coefficient to attain reasonable near-wall asymptotic behavior. The results

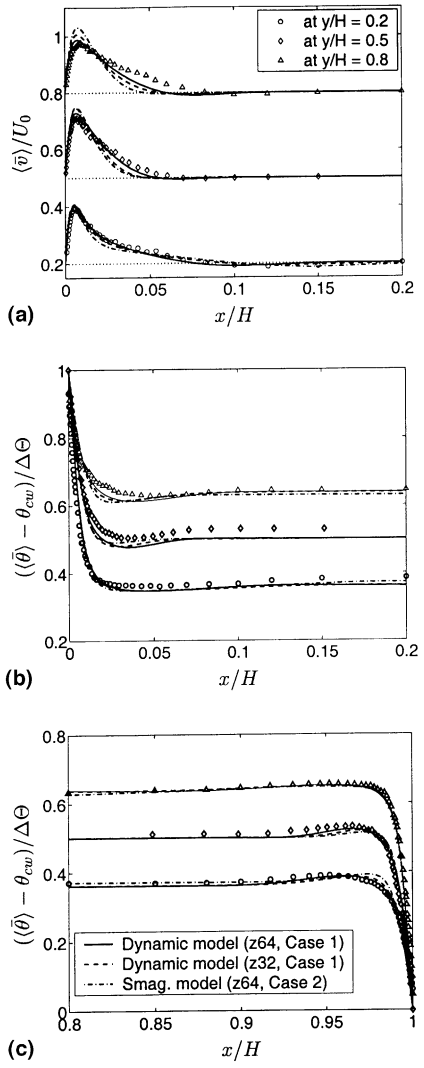


Fig. 1. Comparison of predictions (symbols represent the experimental data): (a) mean vertical velocity near the hot wall; (b) mean temperature near the hot wall; (c) mean temperature near the cold wall.

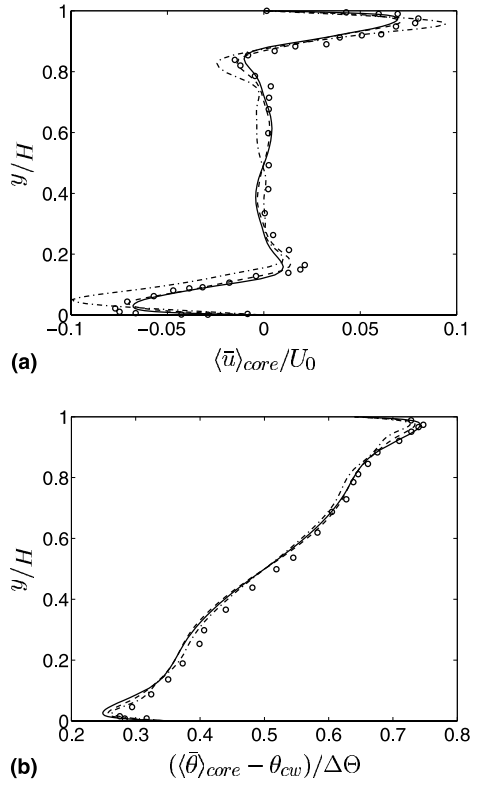


Fig. 2. Comparison of vertical profiles at $x/W = 0.5$: (Same legend for the lines as in Fig. 1 and symbols represent the measured data.) (a) mean horizontal velocity; (b) mean temperature.

computed by this model are generally worse than those given by the dynamic model. As expected, the dynamic model with the fine spanwise grid resolution (z64) yields the best results for the mean flow quantities.

Figs. 2(a) and (b) show the distributions of the mean horizontal velocity component and temperature along the vertical centerline at $x/W = 0.5$. The dynamic model underpredicts the near-wall velocity peak, while the Smagorinsky model overpredicts it. Away from the near-wall flow, unlike the experimental observation which claimed a stationary core region, the simulation produces weak circulation there. This is partly reflected by the wavy profile of the horizontal velocity component along the vertical centerline (Fig. 2(a)). This will be further illustrated in Fig. 4 by visualizing the overall mean flow field. There is no significant variation observed between the results for the mean temperature given by different approaches, as seen in Fig. 2(b). As the wall condition is specified at the spanwise boundaries (i.e., Case 2), the antisymmetrical flow feature about the vertical centerplane is somewhat altered. This can be seen from the results given by the Smagorinsky model in Fig. 2(a). The flow near the bottom wall has a larger magnitude of the horizontal velocity peak than that near the top wall, out of which the backflow is more intensive, however. In addition, it was found at the mid-height ($y = H/2$) that the upward flow near the hot wall in the mid-depth section ($z = D/2$) is somewhat weaker than in the side sections between the spanwise end wall and the $z = D/2$ plane, while the downward flow near the cold wall is stronger in the $z = D/2$ section than in the side sections. This implies that in the $z = D/2$ section the flow in this case (with end walls) to some extent exhibits three-dimensional features.

In Fig. 3, the local Nusselt number, $Nu_l = -(H\partial\langle\bar{\theta}\rangle/\partial n|_w)/\Delta\Theta$, and the wall friction coefficient, $C_f = \langle\tau_w\rangle/(\rho U_0^2/2)$, are compared with the experimental data. No experimental data are available for $C_f$ along the top and bottom walls. At the earlier stage of the boundary layer flow along the vertical walls, the simulation yields lower heat transfer and larger wall friction than the measured data. It should be noted that negative values appear in both $Nu_l$ and $C_f$ along the top and bottom walls, as seen in Figs. 3(a) and (b), respectively. This suggests that the convective heat flux changes direction of transfer between the horizontal wall surface and the cavity air shortly after the vertical boundary layer flow turns to the horizontal direction along the conducting walls, at $S/H \approx 1.174$ and $S/H \approx 3.174$ on the top and bottom walls, respectively. The negative wall friction coefficient, $C_f$, Fig. 3(b), is due to the secondary bubbles forming, respectively, in the upper corner near the heated wall and in the lower corner near the cooled wall, as shown in Fig. 5 below. In general, the dynamic model using fine numerical resolution in the spanwise direction reproduces more satisfactory results than are given with the coarse resolution and by the Smagorinsky model as compared with the measured data.

It has been recognized that the dynamic approach may in general improve predictions as compared with a base model using constant model coefficients. This approach dynamically

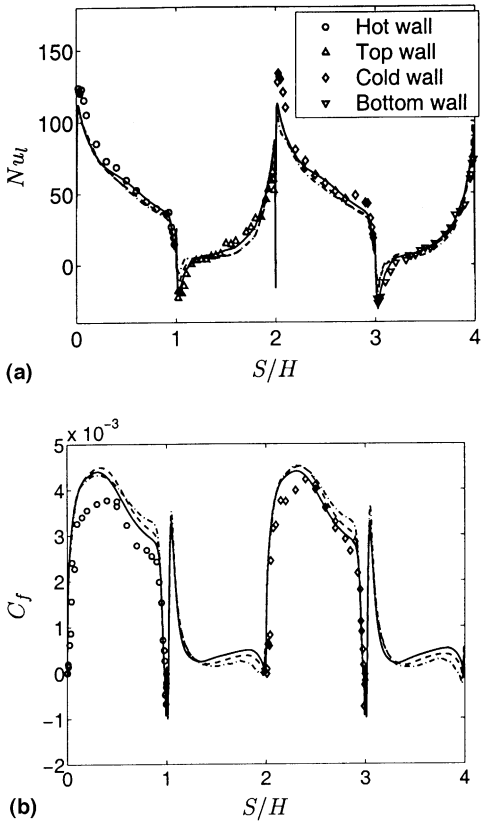


Fig. 3. Predictions of mean wall parameters (starting at $S/H = 0$ from the lower hot corner along the cavity closure surface, $S$, clockwise). Same legend for the lines as in Fig. 1 and symbols represent the measured data: (a) local Nusselt number; (b) wall friction coefficient.

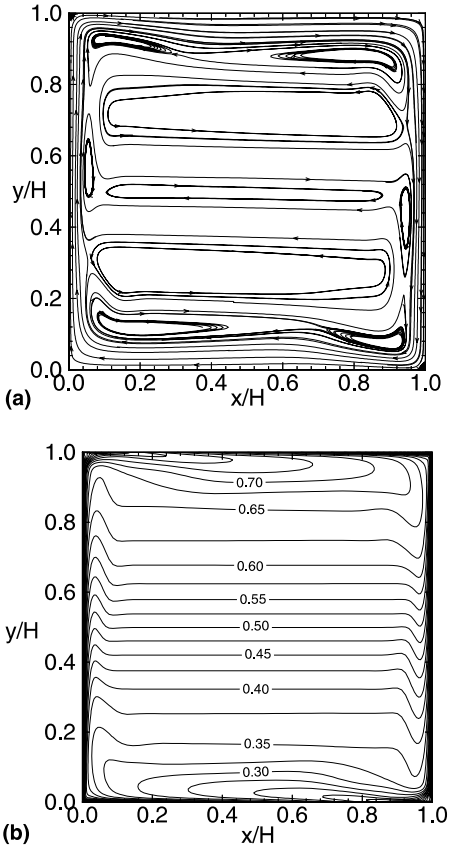


Fig. 4. Mean flow and thermal fields: (a) mean flow streamlines; (b) isothermal lines, normalized as $(\langle\bar{\theta}\rangle - \theta_{cw})/\Delta\Theta$.

determines the model coefficient as a function of time and space in terms of smallest resolved scales. By an additional means (via the model coefficient), the dynamic approach helps to relax the *sharp* requirement imposed on the adjustment of large-scales as in an eddy-viscosity based SGS model (via, e.g., only $|\bar{S}|$ in the Smagorinsky model) that uses constant model coefficients to represent the interaction between the resolved scales and the SGSs. Another reason for the relatively large discrepancy incurred in the results given by the Smagorinsky model is that the spanwise grid resolution has been rather coarse because the numerical domain size in this direction has been doubled in Case 2 compared to Case 1, with two end walls specified as in the experiment. When using the Eidson model, Eq. (5), in Case 1 with the fine grid resolution (z64), where $C = 0.0441$ and $Pr_t = 0.4$, it was found that this model yields even worse predictions than does the Smagorinsky model using the same model constants. The Eidson model generally overestimates the mean flow quantities and turbulence statistics (the results are not shown here). The flow is stratified with a statistically positive temperature gradient in the vertical direction. The buoyancy-related term in the Eidson model, Eq. (5), will thus reduce the SGS eddy viscosity and, consequently, increase the turbulence intensity of the resolved large-scales as found in the simulation. It suggests that model constants different from the Smagorinsky model should be specified for the Eidson model, e.g., using a larger SGS Prandtl number and/or a larger $C$ to enhance the SGS effect.

The dynamic model has shown relatively better behavior as compared with the Smagorinsky model and the Eidson model. In the following discussion, we concentrate only on the results given by the dynamic model for Case 1. Fig. 4 illustrates the streamlines and the isothermal lines, which were computed using the fine spanwise grid resolution (z64). It shows that the flow retains a fairly good antisymmetrical feature. There exist several recirculating regions away from the near-wall boundary layer flows. The rolls next to the wall flows are comparatively strong. With increasing Rayleigh numbers, the boundary layer flow may be more intensive and the neighboring rolls are expected to merge with each other to form a large recirculting motion around the core region. A tiny bubble exists in the top hot corner and in the bottom cold corner. No recirculation is predicted in the other two corners, as identified in the experiment (Tian, 1997).

Fig. 5 presents the close-up illustrations of the mean flow in the two corners near the cold wall. Provided that the flow along the horizontal wall surface is intensive enough, a secondary vortex should be formed in the corner when approaching the opposite vertical wall. This is not the case here, however, as shown in Fig. 5(a). The flow along the horizontal top wall is affected by both the wall shear and the upward buoyancy. As approaching the vertical cold wall, the boundary layer is suppressed by the buoyancy in the vertical direction, and its momentum is consumed by the wall shear in the horizontal direction. Consequently, no secondary vortex is formed in the upper cold corner. When the flow along the vertical cold wall approaches the horizontal bottom wall, the buoyancy in the corner is upward (the bottom wall is a conducting boundary) and thus acts to reinforce the secondary recirculation bubble.

The distributions of the resolved velocity and temperature fluctuations are plotted in Figs. 6 and 7, respectively, where the fluctuation of a quantity, $\phi$, is defined by $\phi' = \bar{\phi} - \langle\bar{\phi}\rangle$. In contrast to the mean flow predictions, these computed

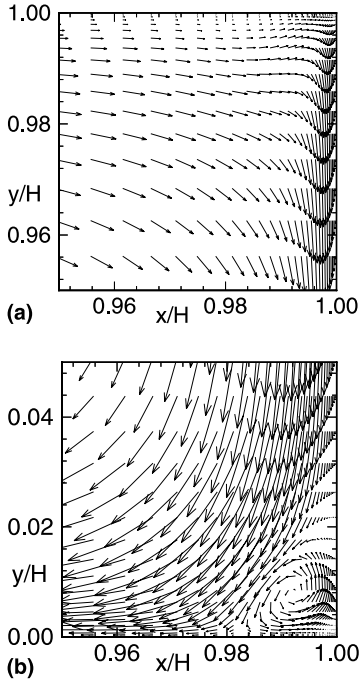


Fig. 5. Mean flow in the two corners neighboring the cold wall: (a) mean flow in the top cold corner; (b) mean flow in the bottom cold corner.

statistics show a relatively large discrepancy in comparison with the measured data (the experimental data for the spanwise velocity fluctuation is not available). The velocity fluctuation in the streamwise (vertical) direction of the boundary layer however agrees reasonably well with the experiment, as shown in Fig. 6(b). The level of the horizontal velocity fluctuation, $\sqrt{\langle u'^2\rangle}$, is on the overall underpredicted as compared with the experiment, see Fig. 6(a). It seems that the wall-damping effect has not been properly resolved. In the outer shear layer between the near-wall flow and the core region, the resolved turbulence statistics for velocities are generally underpredicted while the resolved thermal fluctuation is overpredicted, as seen in Fig. 7.

Also underpredicted is the resolved turbulent shear stress, $\langle u'v'\rangle$, in the outer region, as shown in Fig. 8(a). This suggests that an adequate modeling of the flow in this outer layer is probably as important as that in the vicinity of the wall. In Figs. 8(b) and (c), the distributions for the resolved turbulent heat fluxes are also plotted, although no experimental data are available for comparison. The effect of the grid resolution in the homogeneous spanwise direction is also shown in Figs. 6–8. In general, the grid resolution significantly affects the prediction. This is particularly true for the resolved shear stress and heat fluxes. The temperature fluctuation shows much less sensitivity to the numerical resolution, however, as shown in Fig. 7. A coarse mesh in the homogeneous direction, $96 \times 96 \times 32$ mesh (z32), reproduces too small turbulence statistics (except for the resolved horizontal velocity fluctuation) in the outer region of the boundary layer. The variation in the results of using different grid resolutions suggests that it is of importance to use a sufficiently fine numerical resolution in the direction of flow homogeneity in order to appropriately resolve the flow structure in this direction.

Fig. 9(a) illustrates the time-averaged contribution of SGS shear stress to the total shear stress, $\langle u'v'\rangle_{\text{tot}} = \langle u'v'\rangle_{\text{res}} + \langle u'v'\rangle_{\text{sgs}}$, at location $y = H/2$. A similar illustration is shown in

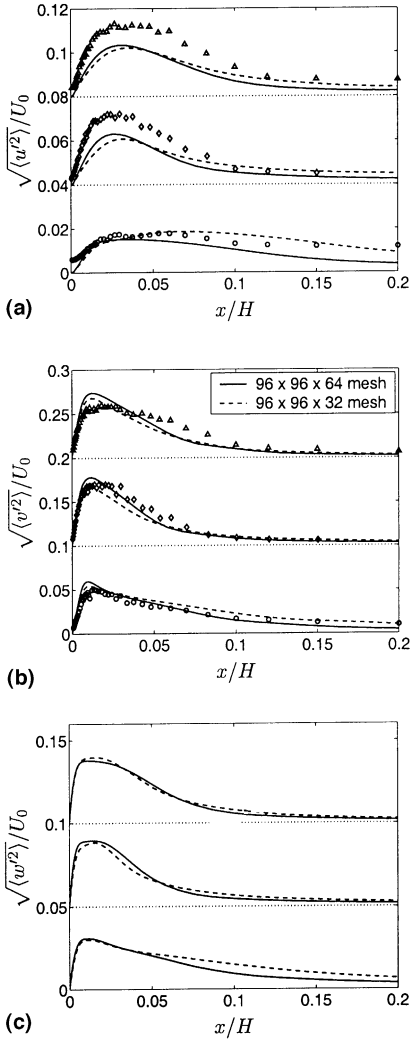


Fig. 6. Resolved velocity fluctuations computed with the dynamic model for Case 1 at $y/H = 0.2$, 0.5 and 0.8 from bottom to top, respectively. Symbols represent the measured data at different $y/H$ levels.

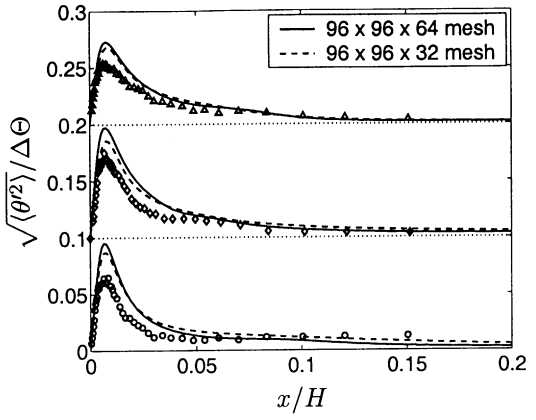


Fig. 7. Resolved temperature fluctuation computed with the dynamic model for Case 1 at $y/H = 0.2$, 0.5 and 0.8 from bottom to top, respectively. Symbols represent the measured data at different $y/H$ levels.

Fig. 9(b) for the horizontal heat flux. The SGS part is significantly smaller than its resolvable counterpart. The most visible SGS contribution is not in the vicinity of the wall but in the

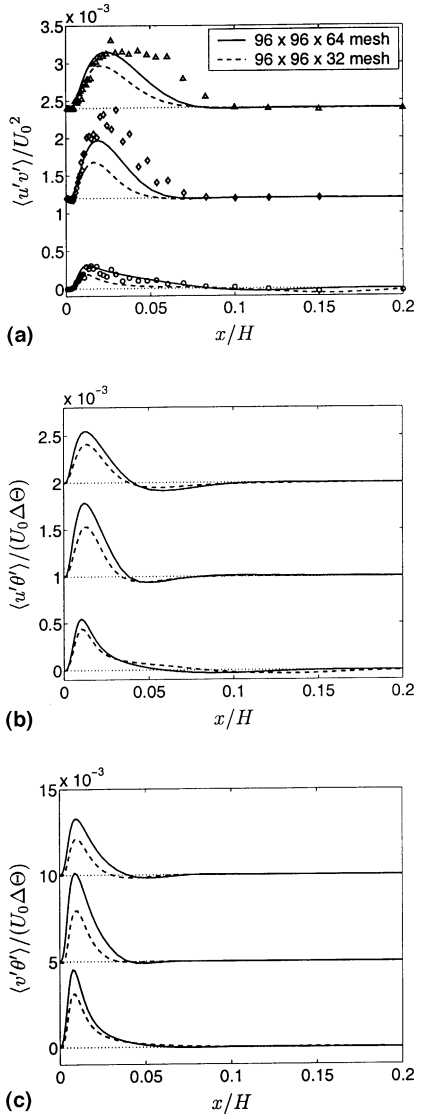


Fig. 8. Resolved turbulent shear stress and heat fluxes computed with the dynamic model for Case 1 at $y/H = 0.2$, 0.5 and 0.8 from bottom to top, respectively. Symbols represent the measured data at different $y/H$ levels.

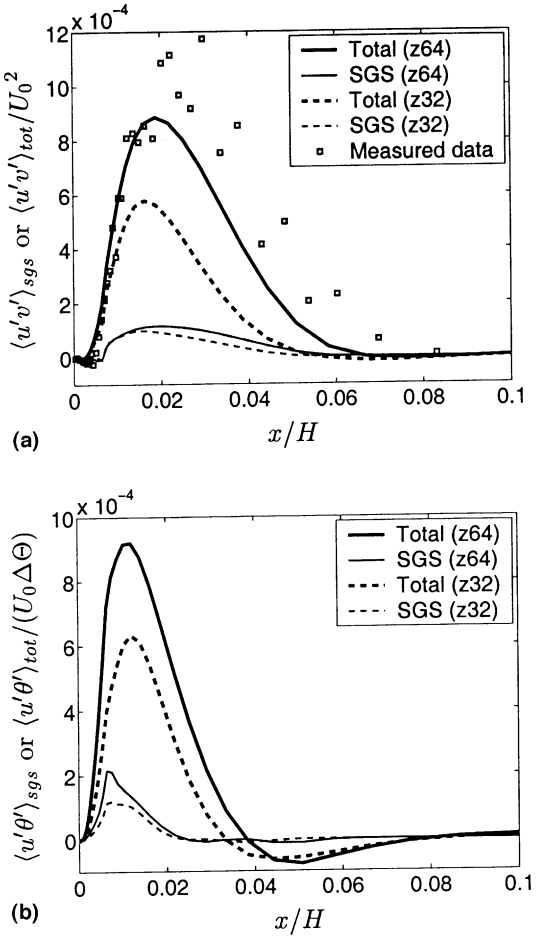


Fig. 9. Time-averaged SGS contribution, profiles at mid-height $y = H/2$: (a) SGS contribution to the shear stress; (b) SGS contribution to the horizontal heat flux.

region about the maximum velocity in the boundary layer. While the spanwise grid resolution significantly affects the resolved turbulence statistics, its influence on the SGS contribution is relatively small. The figure shows that a coarse mesh only in the homogeneous direction (z32) (and thus a 26% larger filter width than with the fine mesh (z64)) does not render a large SGS viscosity because the dynamically determined model coefficient, $C$, becomes small with the coarse mesh in this case.

At the mid-height ($y = H/2$) the linear viscous/conductive sublayer in the vertical boundary layer is located approximately within $x^+ < 3.5$, which is identical with the measurement. Fig. 10 shows the detailed flow structure in the viscous/conductive sublayer close to the hot wall (at $x^+ = 2$ or $x/H \approx 0.001$ within which six nodes are included) by plotting the contours of instantaneous $v'$ and spanwise vorticity, $\omega_z' = (\partial v'/\partial x - \partial u'/\partial y)$ for which the positive values are contoured by solid lines and negative values by dashed lines. The regions with large positive values of $\omega_z'$ in Fig. 10(b) are associated with those consisting of positive values of $v'$ in Fig. 10(a). The flow seems to have a tendency to exhibit some coherent structures similar to the streaks in a forced convection boundary layer (Moin and Kim, 1982), but they are not as extensively elongated. Away from the horizontal top/bottom walls, the structure with positive $v'$ and negative $v'$ (indicated by high concentration contour lines) emerges alternatingly in the spanwise direction. A further visualization of the contour of instantaneous $u$ close to the vertical hot wall shows that the structures with negative and positive values of $v'$ correspond to the sweep ($u < 0$) and ejection ($u > 0$) events, respectively. To resolve the near-wall, streak-like structures, a sufficient grid resolution is required in the spanwise direction. Nevertheless, it should be noted that the buoyant flow considered here is characterized by relatively low velocities along the enclosure surface. Some preliminary analyses of the simulations indicated that the near-wall flow exhibits other different features from a forced convection boundary layer. The streak-like structure having positive $v'$ is not inclined with respect to the wall. A quantitative investigation should be carried out in future work to identify the properties of the flow structures as such in natural convection boundary layers.

The streak-like structure disappears in the vicinity of the horizontal top wall, as shown in Fig. 11 on a $x$–$z$ plane at $y^+ = 0.5$ close to the top wall. Near the hot wall (on the left-hand side), a very narrow region with large values of $u'$ exists owing to the vertical boundary layer flow impinging on the top wall, as seen in Fig. 11(a). The excess momentum in this flow is

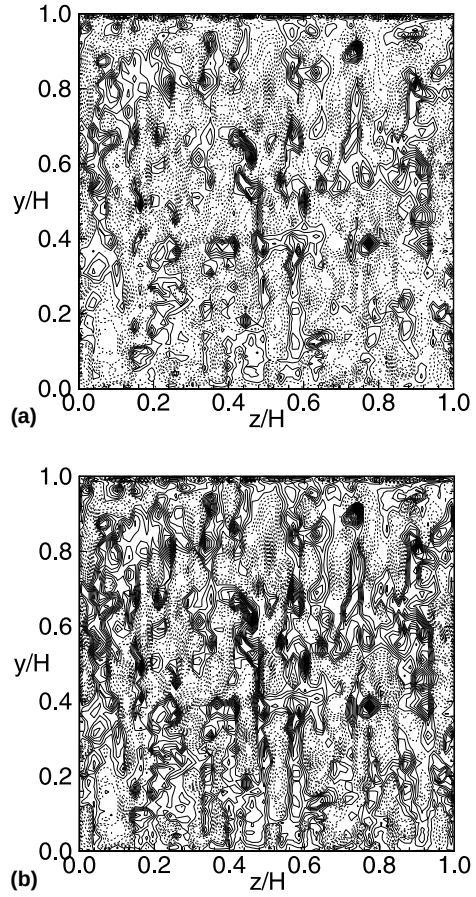


Fig. 10. Contour of $v'$ and $\omega_z'$ at a $y$–$z$ plane near the vertical hot wall at $x^+ = 2$ ($x/H \approx 0.001$) based on the wall friction velocity at $y = H/2$ for Case 1 and z64: (a) contour of $v'$; (b) contour of $\omega_z'$.

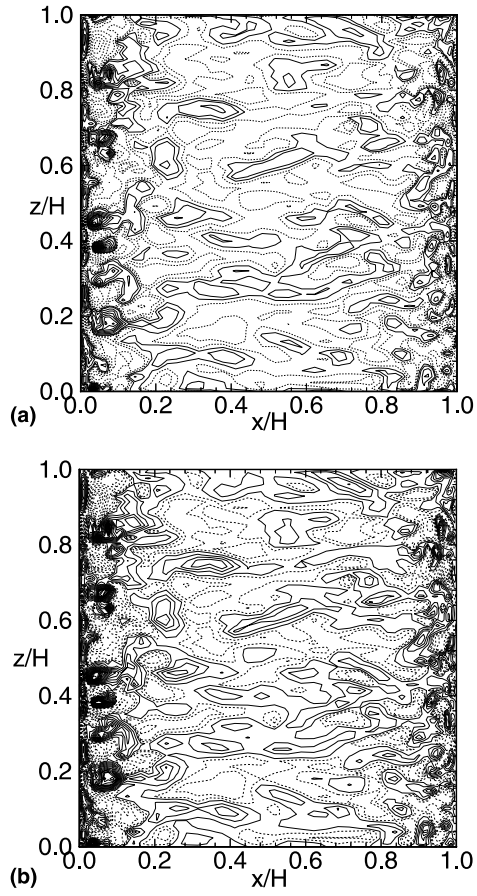


Fig. 11. Contour of $u'$ and $\omega_z'$ at a $x$–$z$ plane near the top wall, at $y^+ = 0.5$ based on the wall friction velocity at $x = W/2$ for Case 1 and z64: (a) contour of $u'$; (b) contour of $\omega_z'$.

however quickly exhausted, and the flow tends to be relaminarized. Moreover, without showing an illustration here, it was found in the simulation that energy backscatter occurs (detected by negative $\nu_t$) in the lower hot and upper cold corners where the vertical boundary layer flows start, as well as in the shear layer of outer region of the boundary layer. In a small region of the two corners, even the time-averaged SGS viscosity retains negative values. It implies that the local flow frequently undergoes a net energy transfer from the subgrid scales to the resolvable scales.

## 4. Conclusions

A turbulent buoyant flow in a cavity with two differentially heated side walls was studied using LES techniques. The flow is characterized by a relatively low turbulence level and thermal stratification. In general, the simulation is able to reasonably reproduce the global mean flow and thermal field, as validated in the experiment. The Smagorinsky model (without being incorporated into the dynamic procedure) reproduces results in larger discrepancies than does the dynamic model as compared with the experimental data. This is particularly the case in the shear layer between the wall boundary layer flow and the cavity core region. The dynamic model is able to yield mean flow quantities that are in rather good agreement with the measured data, although not as good for some turbulence statistics.

The discrepancies between the experimental data and the computed results in the outer part of the boundary layer suggest that special attention should be paid to the flow physics and numerical treatment in this region. Moreover, it was demonstrated that the numerical resolution in the homogeneous direction is of importance for reasonable resolution of near-wall flow structures to get better predictions. A coarse grid resolution (and thus a large filter width relating to the box filter) in the direction of flow homogeneity may not numerically yield large SGS viscosity because the dynamically determined model coefficient may become small. Similar to the streaky structures in a forced convection boundary layer, the natural convection boundary layer flow along the heated/cooled vertical walls tends to exhibit streak-like structures in the near-wall region, but these structures are not as elongated and have less spatial extension at such a low Rayleigh number as is considered in this work. However, in the boundary layer near the horizontal walls, no such structures are detected, where the flow instead tends to be relaminarized.

## Acknowledgements

This work was partly supported by TFR, the Swedish Research Council for Engineering Sciences. The authors are grateful to Dr. Y.S. Tian for providing the experimental data. Computer time on the SGI ORIGIN 2000 machines at UNICC, Chalmers, is gratefully acknowledged.

## References


Cabot, W., 1992. Large-eddy simulations of time-dependent and buoyancy-driven channel flows. In Annual Research Briefs 1992, Center for Turbulent Research, Stanford Univ./NASA Ames Research Center, pp. 45–60.

Canuto, V.M., Dubovikov, M.S., Dienstfrey, A., 1997. A dynamic model for turbulence: IV. Buoyancy-driven flows. Phys. Fluids A 9, 2118–2131.

Cheesewright, R., King, K.J., Ziai, S., 1986. Experimental data for the validation of computer code for the prediction of two-dimensional buoyancy cavity flows. In: Humphrey J.A.C. et al. (Eds.), Significant Questions in Buoyancy Affected Enclosure or Cavity Flows. ASME HTD 60, pp. 75–81.

Davidson, L., 1997. LES of recirculating flow without any homogeneous direction: a dynamic one-equation subgrid model. In: Hanjalić, K., Peeters, T.W.J. (Eds.), Second International Symposium on Turbulence Heat and Mass Transfer, vol. 2. pp. 481–490.

Deardorff, J.W., 1973. The use of subgrid transport equations in a three-dimensional model of atmospheric turbulence. ASME J. Fluids Eng. 95, 429–438.

Dol, H., Hanjalić, K., Kenjeres, S., 1997. A comparative ssessment of the second-moment differential and algebraic models in turbulent natural convection. Int. J. Heat Fluid Flow 18, 4–14.

Eidson, T., 1985. Numerical simulation of the turbulent Rayleigh–Bénard problem using subgrid modelling. J. Fluid Mech. 158, 245–268.

Germano, M., Piomelli, U., Moin, P., Cabot, W., 1991. A dynamic subgrid-scale eddy viscosity model. Phys. Fluids A 3, 1760–1765.

Henkes, R.A.W.M., Hoogendoorn, C.J., 1995. Comparison exercise for computations of turbulent natural convection in enclosures. Numer. Heat Trans. Part B 28, 59–78.

Lilly, D., 1992. A proposed modification of the Germano subgrid-scale closure method. Phys. Fluids A 4, 633–635.

Manson, P.J., 1989. Large-eddy simulation of the convective atmospheric boundary layer. J. Atmos. Sci. 46, 1492–1516.

Moeng, C.-H., Rotunno, R., 1990. Vertical-velocity skewness in the uoyancy-driven boundary layer. J. Atmos. Sci. 47, 1149–1162.

Moin, P., Kim, J., 1982. Numerical investigation of turbulent channel flow. J. Fluid Mech. 118, 341–377.

Peng, S.-H., Davidson, L., 1998a. Comparison of subgrid-scale models in LES for turbulent convection flow with heat transfer. Turbulent Heat Trans. 2, 5.24–5.35.

Peng, S.-H., Davidson, L., 1998b. Large eddy simulation for turbulent buoyant flows induced by differentially heated vertical walls. Report 98/8, Department of Thermo and Fluid Dynamics, Chalmers University of Technology, Gothenburg.

Peng, S.-H., Davidson, L., 1999. Computation of turbulent buoyant flows in enclosures with low-Reynolds-number $k$–$\omega$ models. Int. J. Heat Fluid Flow 20, 172–184.

Smagorinsky, J., 1963. General circulation experiments with the primitive equations: I. The basic experiment. Mon. Weather Rev. 91, 99–165.

Tian, Y.S., 1997. Low turbulence natural convection in an air filled square cavity. Ph.D. thesis, South Bank University, London, UK.